Environmental Science & Technology

Article

Cite This: Environ. Sci. Technol. 2018, 52, 13306−13313

pubs.acs.org/est

Nondestructive 3D Imaging and Quantification of Hydrated Biofilm-Sediment Aggregates Using X-ray Microcomputed Tomography

Naiyu Zhang,[†] Charlotte E. L. Thompson,[*,†,△] Ian H. Townend,[†] Kathryn E. Rankin,[‡] David M. Paterson,[§] and Andrew J. Manning[∥,⊥]

[†]School of Ocean and Earth Science, National Oceanography Centre, University of Southampton, Southampton SO14 3ZH, U.K.

[‡]μ-VIS X-ray Imaging Centre, Faculty of Engineering and the Environment, Highfield Campus, University of Southampton, Southampton SO17 1BJ, U.K.

[§]Sediment Ecology Research Group, Scottish Oceans Institute, School of Biology, University of St. Andrews, St. Andrews KY16 8LB, U.K.

[∥]HR Wallingford Ltd., Coasts & Oceans Group, Wallingford OX10 8BA, United Kingdom

[⊥]School of Environmental Sciences, University of Hull, Hull HU6 7RX, United Kingdom

Supporting Information

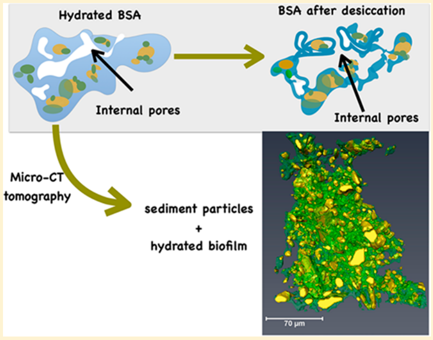

ABSTRACT: Biofilm-sediment aggregate (BSA) contains a high water content, either within internal pores and channels or bound by extracellular polymeric substances (EPS) forming a highly hydrated biofilm matrix. Desiccation of BSAs alters the biofilm morphology and thus the physical characteristics of porous media, such as the binding matrix within BSA and internal pore geometry. Observing BSAs in their naturally hydrated form is essential but hampered due to the lack of techniques for imaging and discerning hydrated materials. Generally, imagery techniques (scanning electron microscopy (SEM), transmission electron microscopy (TEM), and focused ion beam nanotomography (FIB-nt)) involve the desiccation of BSAs (freeze-drying or acetone dehydration) or prevent differentiation between BSA components such as inorganic particles and pore water (confocal laser scanning microscopic (CLSM)). Here, we propose a novel methodology that simultaneously achieves the 3D visualization and quantification of BSAs and their components in their hydrated form at a submicron resolution using X-ray microcomputed tomography (μ-CT). It enables the high-resolution detection of comparable morphology of multiphase components within a hydrated aggregate: each single inorganic particle and the hydrated biofilm matrix. This allows the estimation of aggregate density and the illustration of biofilm-sediment binding matrix. This information provides valuable insights into investigations of the transport of BSAs and aggregate-associated sediment particles, contaminants (such as microplastics), organic carbon, and their impacts on aquatic biogeochemical cycling.

1. INTRODUCTION

Sediment particles in aquatic environments provide suitable solid−liquid interfaces for microorganism (e.g., bacteria, algae, diatom, fungi, and archaea) accumulation.[1] By secreting copious amounts of extracellular polymeric substances (EPS) binding sometimes more than 90% water[2,3] and adhering sediment particles together, these microorganisms form hydrogel-like microorganism-sediment aggregates, defined here as "biofilm-sediment aggregates" (BSAs). These aggregates are extensively present, either in overlying water or as part of a soft or consolidating layer aggregated across the sediment-water interface.[4−6] The internal structure of BSAs reflects microbial mediation on sediment particles, such as by reducing the pore space among particles for flow,[7] rearranging the particle distribution, altering particle/aggregate cohesion mechanism,[8] and absorbing various materials and contaminants including microplastics and nanoparticles, as well as trapping and storing nutrients and microbes.[9] The internal structure of BSAs is critical to the physical transport of BSAs and associated materials, often accelerating the deposition of suspended particulate matter (SPM)[10] and strengthening the resuspension resistance of benthic deposits.[11,12] From an ecological viewpoint, it affects biogeochemical cycling of the nutrients, carbon, and the transport of associated microplastics, nanoparticles, and heavy metals.[13−15]

Fractal theory has been applied to study aggregate structure,[16−18] assuming a self-similar structure that self-repeats at all dimensional scales.[19] However, this is due to a lack of currently available techniques to validate the internal structure of BSAs. Free-settling tests using optical microscopy or camera imaging have been used to collect 2D external morphologies and settling velocities.[20] The porosity, permeability, or density cannot be directly measured but instead are estimated by Stokes' law,

Received: July 27, 2018
Revised: October 16, 2018
Accepted: October 24, 2018
Published: October 24, 2018

DOI: 10.1021/acs.est.8b03997

erroneously assuming a homogeneous and impermeable internal architecture.[21]

A single BSA is an EPS-bound network usually consisting of several associated microaggregates/clusters (≤10 μm) in different development stages.[22] EPS is present in various forms, including colloidal, capsular, surface film, or fibrous.[2,23] If confirmed, a highly heterogeneous internal mass distribution within BSAs would challenge the use of Stokes' law or fractal theory to represent the "true" biofilm-sediment binding nature[24] of BSA.

Scanning Electron Microscopy (SEM) has been used to image EPS strands and plates; however, the standard SEM requires dehydrating the hydrated samples, unavoidably resulting in considerable distortion of hydrated biofilm matrix.[25] Low-temperature SEM (LTSEM) or cryo-SEM requires freezing of fully hydrated biofilm, which has been proven to cause considerable artifacts, thereby making it difficult to interpret the biofilm binding mechanisms.[26] Transmission electron microscopy (TEM) is another technique for a high-resolution imaging of EPS fibril bundles in BSAs but only for 2D observation.[27] Focused Ion Beam Nano tomography (FIB-nt) has recently been used for 3D characterization of the structure of suspended flocculated matter.[24] However, as with TEM, the FIB-nt technique requires aggregates to be dehydrated and stabilized in resin blocks. The preparatory losses of EPS during conventional resin-embedding methods is considerable, sometimes accounting for 50%−80%.[28]

Either SEM or TEM/FIB-nt involves various degrees of desiccation of BSAs, rather than direct 3D imaging of hydrated BSAs in liquid media. Biofilms in natural BSAs are predominantly comprised of water,[3] and the majority (up to 98%)[3] bound by EPS within the biofilm matrix can be easily removed.[3] Prior work has shown that biofilms create an environment which can retain moisture.[2] When biofilms are exposed in dry environments, the loss of water at the biofilm surface brings polymer sites closer together,[8] forming a skin-like protector against further evaporation of the water underneath.[2,8] The binding architecture is altered, and the internal pores and channels are distorted. The observed structure of BSAs undergoing desiccation is thus unlikely to be representative of the structure of the samples when they transport in fully hydrated form.[25] Given that fluid flow through BSA pores and channels is a key mechanism for uptake, storage, and mineralization of carbon and nutrients from surrounding environments,[29] a realistic observation of the flow pathways through BSA is crucial for investigating nutrient exchange,[30] entrapping, and accumulation of microbes in such porous media[8] and fully understanding the function of BSA. Conducting nondestructive, 3D imaging and quantification of hydrated BSA sustained in liquid medium is therefore important.[31] Environmental SEM (ESEM) and confocal laser scanning microscopic (CLSM) in combination with fluorescent staining are two of the most promising currently available tools for observing a hydrated biofilm matrix.[32] However, ESEM is limited to the characterization of surface structure, instead of the 3D internal structure (pores and channels), while CLSM fails to distinguish the morphology of sediment particles and pore water in aggregates as neither can be targeted by appropriate staining.[33]

These standard specimen preparation techniques provide limited aggregate imaging to date, and the direct imaging of hydrated aggregates in liquid media would be a preferable approach. The objective of this work was to introduce a methodology which could achieve direct imaging of aggregates in their hydrated form and be able to distinguish between hydrated biofilm, water, and sediment particles at a high-resolution and in 3D.

X-ray microcomputed tomography (μ-CT) techniques are applied in this work to capture the volumetric characterization of 3D internal structures at the micron scale.[34] While it has been used in prior work in combination with FIB-nt to get the resin-cured flocs, its use has been limited to provide gross-scale information on flocculated materials.[35] To assess the suitability of the technique and design an optimized protocol for imaging, we compared typical BSAs specimen preparation methods, including fast-freezing, resin-embedding, and wet staining. The resulting method proposed simultaneously achieved the nondestructive imaging and quantification of the 3D matrix of BSAs in their hydrated forms. It enables the precise detection of multiphase components within an individual aggregate: individual sediment particles hydrated biofilm matrix and pore water. It also enables the estimation of density of individual aggregates and the detection of the biofilm-sediment binding matrix. The imaging period was successfully optimized to 3 h for a submicron resolution, significantly improving cost effectiveness.

2. MATERIALS AND METHODS

Simplified, replicable laboratory-cultivated alga-kaolinite aggregates were generated and used to ensure reproducibility and cross comparison among different preparation methods. By which, the ultimate purpose is to investigate the best methodology for imaging. Work flows from aggregate creation through to image acquisition and processing are explained in the following section.

2.1. Biofilm-Sediment Aggregate Creation. A commercially available kaolinite powder (ACROS Organics, 1−1.8 μm) was fully saturated in distilled water before use and placed under vacuum to eliminate potential hydrophobic effects caused by air bubbles on particle surfaces.[36] Primary particle size distribution (PSD) was measured using a LS300 Coulter laser[37] for later comparison with primary particle size of the created aggregates using imaging analyzing. The algae, *phaeodactylum tricornutum*, was used as a single species for aggregation (cultured in the Research Aquarium Laboratory, National Oceanography Centre, Southampton (NOCS)). The alga was cultured in artificial seawater (Sigma sea salts, salinity 35 ppt) with added nutrients (sodium metasilicate) and added sodium hypochloride, to inhibit bacterial growth in order to simplify the whole system (10:5:2). The culture solution was left illuminated for 24 h at 18 °C, after which 1.25 mL of sodium thiosulfate was added to neutralize the pH. After this, 100 mL of kaolinite and 100 mL of algal suspension were added and gently mixed. After a 6-day incubation period, aggregates were found suspended in the water column and formed a fluff layer at the bottom of the incubation vessel. Aggregates at the surficial fluff layer were easily resuspended through gentle agitation. Aggregates were sampled using a wide-mouthed pipet and immediately underwent specimen preparation protocols in order to minimize sampling artifacts.[38] The sampled aggregate size range and shape were also obtained using a camera-imaging system during settling tests[20] and found to have a size range of 15.8−593.0 μm and a height to width ratio of 0.3−3.0.

2.2. Aggregate Specimen Preparation. Different BSA specimen preparation methods for μ-CT were chosen and compared, to assess the suitability for imaging. The ultimate purpose of each preparation method was to sustain the fully hydrated matrix of aggregates.

2.2.1. Liquid Nitrogen Freezing of Aggregates. Liquid nitrogen (LN_2) was used as a high-speed freezing treatment to

DOI: 10.1021/acs.est.8b03997
Environ. Sci. Technol. 2018, 52, 13306−13313

minimize the freezing artifacts.[39] Fresh aggregate samples were placed in a 20 mL plastic syringe (radius 2 cm and depth 3 cm) and immediately immersed into an LN_2 pool at −196 °C for 2 min, which ensured that the aggregates were sufficiently frozen.[40] The frozen aggregates were not dried, as while drying preserves the fibril bundles of biofilms, it does not sustain the hydrated polymers in BSAs.[26] As thawing of the frozen samples can cause significant displacement of features inside the specimen, the specimen vial was held in dry ice during scanning.

2.2.2. Embedding Aggregates in Resin. A 3 mm-diameter hole (3 mm depth) in a preprepared pure resin block was created in advance to hold aggregates that were carefully transferred into the hole immediately after creation. The embedding of the aggregates in resin was carried out following standard preparation procedures[24] (with the main steps summarized herein). As epoxy resin is hydrophobic, the aggregates were repeatedly soaked in anhydrous acetone to replace the internal water. This is followed by resin filtration, after which the sample was cured at 60 °C. A 5*5*5 mm resin sub-block containing the target aggregates was sectioned for whole-volume scanning to avoid artifacts during alignment of the sectioned image series to a 3D data set.

2.2.3. Wet Staining Aggregates. A sealed 200 μL pipet was used as the specimen container for wet aggregates. The pipettes are composed of polypropylene ensuring low X-ray absorption. The thin walls (200−300 μm)[41] of the container allow for minimization of the amount of media between the aggregate target and the detecting probe, reducing extra X-ray absorption.[42] One of the most challenging problems for wet aggregate scanning is to stabilize aggregates in the liquid media during the entire scanning process which can last several to dozens of hours. To address this from a specimen preparation approach, initial attempts were made to stabilize the samples in an absolute alcohol treatment. The alcohol treatment aims to immobilize the algae cells and the production of bubbles by algae activities, which can cause irreparable failure in image reconstruction. Following the alcohol treatment, Alcian blue dye solution was added in specimen for a 7 min staining period which has been reported as sufficient.[43] Alcian blue has been used in several studies investigating the size, form, and abundance of acidic polymeric substances (APS) which contribute significantly to biofilm adhesion.[44,45] Alcian blue (Sigma; 0.4 wt %/wt at pH 2.5)[43] was sonicated for 15 min to disaggregate the particles and then passed through a 0.45 μm filter twice to remove stacked particles and ensure a homogeneous solution.

3. BSA IMAGING AND IMAGE PROCESSING

The LN_2 frozen aggregates packed around by dry ice were imaged with X-ray micro-CT using a modified 225 kVp Nikon HMX ST, while the 3D imaging of BSAs embedded in resin and in liquid (stained and unstained) was conducted using a Zeiss 160 kVp Versa 510 X-ray microscope, both located at the μ-VIS X-ray Imaging Centre, University of Southampton. The latter scanner uses a two-stage magnification approach, combining the geometric magnification of the X-ray cone beam and source-to-detector/object distances, with optical magnification through a microscope lenses system to further magnify the image ahead of the detector (Figure 1c). μ-CT scanning protocols for each BSA specimen are listed in Text S1, Supporting Information. In the reconstructed stack images, voxel intensity (grayscale value) reflects the variation in X-ray absorption, which is a function of the material's physical and radio-density throughout the volume.[46] In summary, it can be inferred that brighter pixels represent denser materials (e.g., sediment in this case), while darker pixels represent less dense materials (biofilm and pore water)[47] (Figure 1d). Details of the density calibration and estimation protocols are explained in section 4.5.

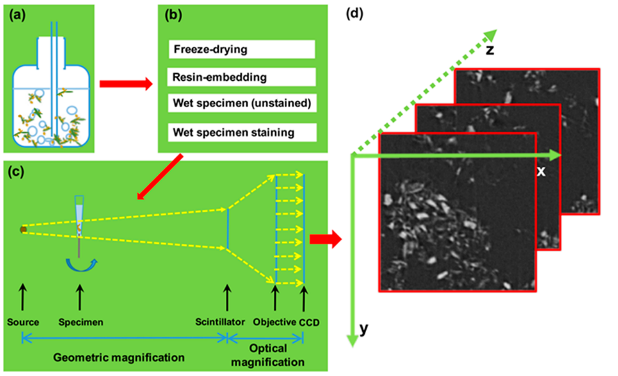

Figure 1. Schematic illustrations of workflow from BSAs creation (a), sampling and BSA specimen prepared using a full range of available protocols (b), to X-ray micro-CT setup (c). Illustrates the dual-magnification imaging system including both the geometric magnification and optical magnification. The resulting reconstructed volumetric slice images composed of different voxel grayscale values representing the X-ray absorption map throughout the volume which is closely relevant to the material density variations (d).

Multipurpose image processing was conducted using Avizo 9.3.0 software (FEI Hillsboro, OR, USA)[48] in cooperation with Fiji/ImageJ (National Institutes for Health, USA),[49] including image filtration and image segmentation. The ultimate purpose was to distinguish different material components (biofilm, pores, and sediment particles in this circumstance) within a BSA. Initially, stack images were cropped to retain one targeted aggregate. In order to increase the accuracy and efficiency of image segmentation, image filtration was conducted using the Avizo 9.3.0 Median Filter to average out image noise. Segmentation relied on a Trainable Weka Segmentation 3D plugin within Fiji/ImageJ, using a collection of visualization tools and machine-learning algorithms based on the user input and then performing the same task in the untested data.[50] By identifying and recognizing targeted objects manually in a subset of images and annotating them to train the classifier, the machine-learning algorithms apply multiple filters to perform particle separation (operation details see https://imagej.net/Trainable_Weka_Segmentation).[24,49] Thereafter, successfully segmented biofilms, pores, and sediment particles could be imported together into Avizo 9.3.0 for subsequent volume rendering, quantitative label analysis, and permeable flow simulation.[51,52]

4. RESULTS AND DISCUSSION

4.1. Comparisons of the Different Specimen Preparation Methods. *4.1.1. LN_2-Freezing Specimens.* Keeping aggregate specimens frozen during the several-hour scanning period was challenging due to the room-temperature scanning environment. Covering the aggregate specimen in dry ice effectively mitigates the temperature difference but increases the distance between the specimen and the X-ray source. As a result, the best achievable resolution is sacrificed. This effect may be minimized by reducing the amount of dry ice used, but then insufficient cooling by a small amount of dry ice would lead to the sample defrosting and therefore scanning failure. Given an average scan time of several hours, it was challenging keeping specimens sufficiently frozen, even without reducing the amount of dry ice used. The best scan provided a 10 μm resolution. No aggregates were captured in the image, which instead indicated a considerable amount of ice crystal formation and air bubbles within the sample (Figure S1, Supporting Information). This showed that high-speed freezing by LN_2 can still result in the formation of ice crystals, and the authors advise caution when using freezing methods to interpret biofilm-sediment binding due to potentially considerable freezing artifacts.[39] As such, freezing aggregates by LN2 was not deemed a suitable specimen preparation method for Micro-CT.

4.1.2. Resin-Embedded Aggregates Scanning. As the aggregates were well stabilized in the resin block, a 20 h long scan was possible, which secured a high-resolution of 683 nm (Figure 2). Although primary particles and sufficient aggregates were detectable, a considerable number of aggregates showed blurred biofilm boundaries (BSAs 4, 5, 6 in Figure 2a). This may be due to the high X-ray absorption properties of resin materials. This prevents a precise discrimination of aggregate morphology, biofilm matrix, or the internal pore geometry against the background resin during subsequent image processing for some samples. Meanwhile, some aggregates show distinct, regular, sharp, and spherical edges (BSAs 1, 2, 3 in Figure 2), as well as an easily detectable biofilm network, which was common in the scans. As widely acknowledged by prior investigations[53] and optical microscopy observation of untreated aggregates (Figure S2, Supporting Information), the shape of aggregates is generally irregular and amorphous, and a regular sphere was not expected. This architecture may result from the preparation procedure during embedding BSAs in resin. The resin should theoretically penetrate into the pores within aggregates to replace the bulk liquid without any perturbation by compression or dehydration.[28] However, the regular and circle-like aggregates observed may indicate that, instead of penetrating these pores, the resin wraps around the aggregate body, possibly due to the nontrivial internal micro/nanopore geometry. Some compression effects on aggregates structure seem unavoidable. Thus, although a dense network of biofilm can sometimes be observed, caution should be taken to interpret the structure and biofilm matrixes of resin-embedded aggregates.

It also should be noted that not all resin penetration into the aggregates failed (blue arrows in Figure 2(b)). In these areas, aggregates have irregular morphology, but this is associated with a low contrast between the biofilm matrix and the surrounding resin. As high noise and low contrast were typical of resulting images, this may be partially caused by the high X-ray absorption of resin materials. However, sufficient contrast can be obtained when the resin fails to completely penetrate into the pores of aggregates but instead forms around the aggregate body (BSAs1, 2, 3 in Figure 2(a)). It is thus clear that the contrast between the saturated biofilm and the resin itself is enough to be detected, and so the low contrast highlighted in the blue-arrowed aggregates may result from the resin-penetrated biofilm. As explained in the introduction, biofilms are predominantly comprised of water, the majority of which is bound by EPS forming the hydrated matrix of biofilm. Such water is easily removed through dehydration and replacement,[3] which are always accompanied by resin penetration and always associated with artifacts (e.g., shrinkage).[25] Therefore, the resin-penetrated biofilm and BSAs were unavoidably altered. In conclusion, embedding hydrated biofilm-sediment aggregates in resin might not be optimal to allow interpretation of the hydrated matrix characteristics, due to the resulting low-contrast, possible compression by resin and partial dehydration.

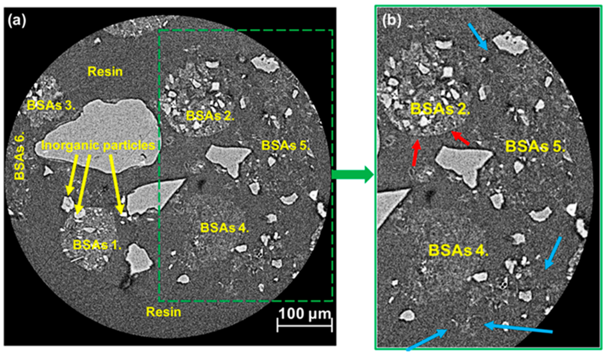

Figure 2. An example image slice of resin-embedded BSAs. The inorganic fine particles and a sufficient amount of aggregates were detected (a): BSAs1, 2, 3 showed a sufficient contrast with surrounding resin, while BSAs 4, 5, 6 showed poor discrimination against surrounding resin and poor discrimination of components. Aggregates with a sufficient contrast present sharp, regular, and curved edges (BSAs2 red-arrow in (b)), while the aggregates with an amorphous shape suffer from a lower contrast with surrounding resin (blue-arrow in (b)).

4.1.3. Wet Specimen Scanning: Stained and Unstained. Stabilizing aggregates in a liquid media remains a problem during the long scanning process. To achieve the best spatial resolutions of 683 nm, a 14 h plus scanning period is typically required. However, initial results indicate that such a scanning period results in considerable movement of the untreated wet aggregates, causing a complete failure of image reconstruction. The consolidation of materials, movement of the algae cells, and the production of bubbles by live algae during scans lasting >14 h can accept considerable movement. The problem is to acquire acceptable scans thus remains as to how to reduce the scanning period without sacrificing image resolution, contrast, and signal-to-noise ratio (SNR). The μ-CT machine parameters were adjusted for conducting a shorter 3-h scan (parameter details are listed in Supporting Information SI1, text S1). However, tests of untreated samples showed significant sample movements even within 2 h.

To avoid resolution sacrifice and the decrease of image quality (e.g., lose the ability to distinguish biofilm matrix), efforts from specimen preparation were also contributed to address this question (Section 2.2.3). Absolute alcohol treatment was applied to immobilize algae cells and minimize their metabolism. Alcian blue treatment was then applied to help discern hydrated biofilm from surrounding pore water. This procedure led to successful images of the wet aggregates. The resulting scanning time was 3 h, with a high-resolution of 777 nm, and allowed for the discrimination of hydrated biofilm from surrounding water and sediment particles. As such, the following results and discussions are all based on the wet scanning of stained specimens prepared in section 2.2.3.

4.2. 3D Models of Hydrated BSAs. In the cross-sectional grayscale raw images (Figure 3a), an image was segmented into different regions (Figure 3b), based on the grayscale values of each voxel using a semiautomatic trainable segmentation tool in Fiji/ImageJ.[51] Grayscale levels reflect the X-ray attenuation degrees which are determined by the densities of different materials.[47] Each constituent of an aggregate, such as sediment particles, biofilm, and water, produces their own specific grayscale ranges (details in section 4.5 and Figure 6) and reflects their different geometries, which enables partition of an aggregate into three component materials. The raw image stacks

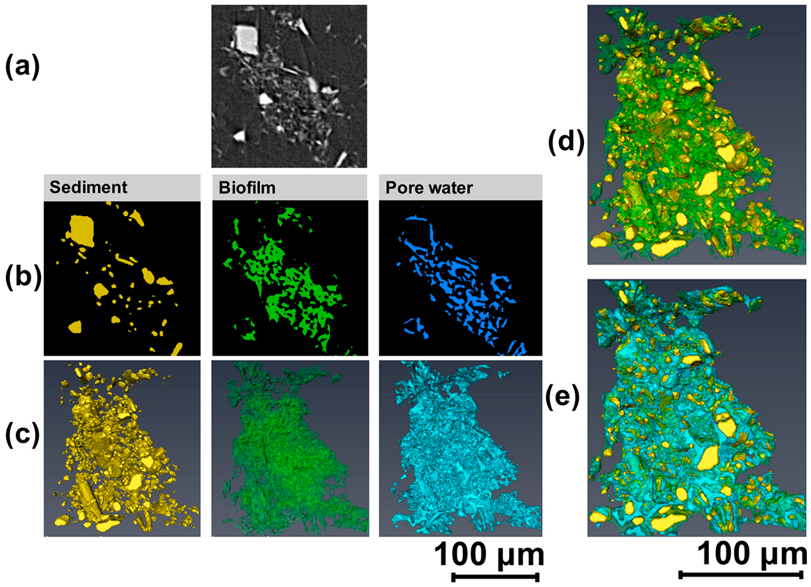

Figure 3. Grayscale raw images (a) processed by image denoising and segmentation to separate aggregate components into biofilm, pores, and sediment particles channels (b). (c) shows a 3D reconstructed model of each constituent by volume. (d) is the 3D view of the distribution of biofilm-sediment in an individual BSA, giving insight into the biofilm-sediment interactions when sustained in water. (e) 3D model of one intact aggregate comprising of each single constituent, including internal pore water.

(2D image slices) of an aggregate were divided into three image stacks: sediment particles, biofilm, and water. Each 2D image stack is then reconstructed to a 3D data set/model by the volume rendering algorithm in Avizo 9.3. (Figure 3c, operation manual[52]). The 3D models of each of the components can then be overlaid to reconstruct the intact aggregate (Figure 3d and 3e). This method avoided BSA desiccation and allows for the discriminantion of internal pores from a comparable matrix of hydrated biofilm.

4.3. Particle Size Distribution (PSD) of Sediment Particles in Aggregates. PSD was measured by labeling sediment particles and conducting label analysis using Avizo 9.3.0. This was compared to more conventional laser sizing data. These two methods are both based on using an equivalent diameter to measure the sediment particle size. The CT-based PSD showed a distribution with a median grain size D_{50} = 4.72 μm (Figure 4a), validated against the Coulter-measured PSD D_{50} (5.11 μm), both of which exceed the size range of the primary particles (1−1.8 μm). Considering that a voxel resolution of 0.777 nm allows the detection of particles within this primary particle size range, this suggests aggregation of the primary clay particles. A comparison of the two data sets shows that D_{10}, D_{25}, and D_{50} all exhibit similar results, while D_{75} and D_{90} showed some differences (Figure 4b). The Coulter-measured PSD showed that particles ranging from 15 to 77 μm account for 12% of the distribution. This significant difference may be due to potential electrochemical interactions among the kaolinite clays enhanced by moderate turbulence[54] during stirring of the sample volume during the Coulter-measurement procedure. However, it may be an artifact of the laser particle sizing model, which equates particle sizes to an equivalent particle diameter. CT based PSD also has the added benefit of direct visualization of 3D architecture of individual sediment particles, enabling further shape geometry analysis of each single particle by image-based programming (e.g., Matlab, developed by MathWorks Inc., USA).[55]

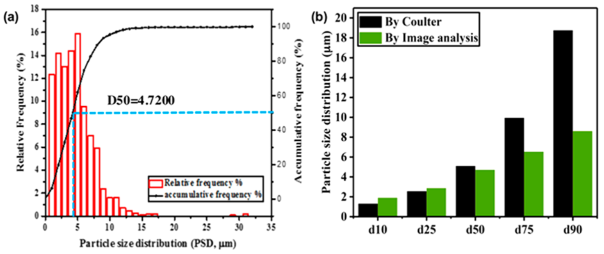

Figure 4. (a) Image-based distribution of sediment particles embedded in biofilm aggregates (PSD, μm). (b) Comparisons between measured PSD by Coulter and PSD by CT image analysis.

4.4. The Hydrated Matrix in Biofilm-Sediment Binding. As discussed above, the water bound by an EPS hydrogel is easily removed. The distortion of the biofilm matrix and the internal geometry of BSAs by dehydration seems largely unavoidable in previous imaging methodologies. Since no desiccation or freezing is involved in the proposed methodology, direct 3D imaging of the wet matrix of biofilm tissues (Figure 5) is possible. The detailed biofilm matrix, including the fabric-like stands and plates and gel-like materials, as well as the matrix voids, is

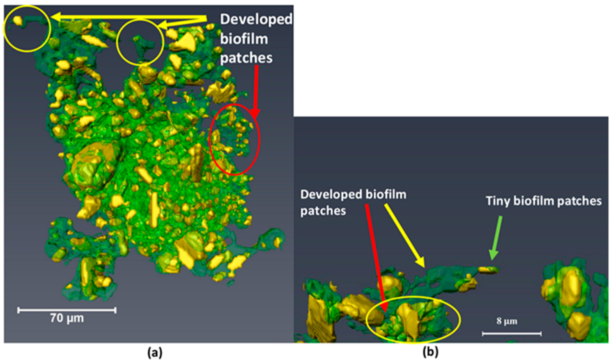

Figure 5. Illustrating different geometries of biofilm-sediment binding matrixes in BSAs.

defined by Flemming[2] as *'a pore or channel in the biofilm matrix that contains liquid water and is not filled with hydrated EPS molecules'*. These voids are important for the uptake and accumulation of nutrients, heavy metals, organic substances, and particles[23] and are especially well represented using this methodology.

This method succeeded in capturing different biofilm-sediment binding matrixes within an individual BSA at a 3D, submicron voxel resolution and in their hydrated form. We note that the majority of sediment particles is bound/bridged by biofilm forming aggregates[27] (Figure 3(c) and (d)). This might be due to the presence of microbial cells, influencing the shape and surface properties of the inorganic particles compared with purely abiotic conditions.[8] Natural aggregates are significantly microbiologically mediated, indicating the importance of appropriately considering the microbial processes in aggregation for large-scale morphodynamic modeling which often consider inorganic aggregates.[56]

This method illustrates the successful capture of tiny biofilm patches attached to sediment particles (green arrow in Figure 5(b)). This may arise as an initial attachment with single cell colonizing the sediment particle surfaces,[9] which is followed by EPS secretion, forming localized biofilm patches.[1,8,57] Alternatively, this might be caused by the breakup of the biofilm bridge with another aggregate. Further investigations apply this method as a straightforward tool to test these hypotheses. Some relatively developed biofilm patches with different geometries have also been observed. Some appear "loosely bound" with a few particles (yellow arrows in Figure 5), while others appear "well packed" with more particles embedding (red arrows in Figure 5). This is consistent with the hypothesized cell colonization patterns of "poorly touched" and "well-touched" mentioned in the studies of biomineral aggregates.[58] Clearly, the mechanisms behind these various biofilm-sediment binding matrixes are still unclear, and the described methodology provides a visual tool for informing and testing these and producing a further understanding of these mechanisms.

4.5. Quantification of BSA Component Density. Gray scale values for each pixel in raw images reflect the variations in the densities of the component materials.[47] Beer's law[59] can be used to relate pixel intensity (grayscale value) to the corresponding density of the biofilm, sediment, and pore water. This takes the form of a linear relationship between the Hounsfield unit (HU, which also reflects a spectrum of X-ray attenuation[59]) and the bulk density of sediment and has been evaluated and successfully applied to approximate sediment density.[46,60] The linear relationship (the slope ratio and intercept) is not constant but varies with spatial variations of the components and structures due to the photoelectric effect.[61] In prior work, the entire specimen was usually assigned a single linear relationship between density and pixel intensity; here the linear relationship was recalibrated within every 10 image slices for the entire 180 slices of the aggregate. The aim is to reduce the potential photoelectric effects caused by spatial disunity of components and structure distribution within one specimen. For each image slice, 10−15 regions of interest (ROI) were selected. The selection of each ROI was strictly specified: only the areas containing all three materials were chosen (Figure 6). This is because we assume the densities and pixel intensities of sediment, biofilm, and pore water within this small area obey the same linear relationship. Comparison of the value of pixel intensity along the transect with material type at the corresponding position allows the average pixel intensity of the sediment, pore water, and biofilm to be estimated and a specific linear relationship to be calculated for each region. The densities of sediment particles and water were measured in advance, and the pixel intensities of all sediment particles, biofilms, and pore water were measured from the raw grayscale images. Based on the densities and intensities of sediment particles and pore water, the linear relationship (intercept and the slope) between pixel intensity and density in the area was calibrated, by which the density of biofilms can thus be calculated (Figure 6). Three of the ten selected ROI lines for one image slice are provided in Figure S4, Supporting Information, each transecting all three different materials. Interestingly, results illustrate that the value of biofilm density in the aggregate is very variable. For example, the biofilm density in the three ROI lines (Figure S4, Supporting Information) varies from 1155 to 1503.19 kg/m^3. This is not surprising, given that the polymers that form biofilm are themselves very variable depending not only on their source and age but also on local physicochemical conditions such as hydration state, molecular bonding, and composition that may change with the nature of available ions that may be absorbed. The biofilm matrix within the aggregate may form initially from microbe clusters. As the growth of these residential microorganisms and the amount of EPS they secrete increase, more particles and microbes are adhered, forming a biofilm-sediment patch. There may also be an element of cell-signaling (quorum sensing) that attracts other colonizers.

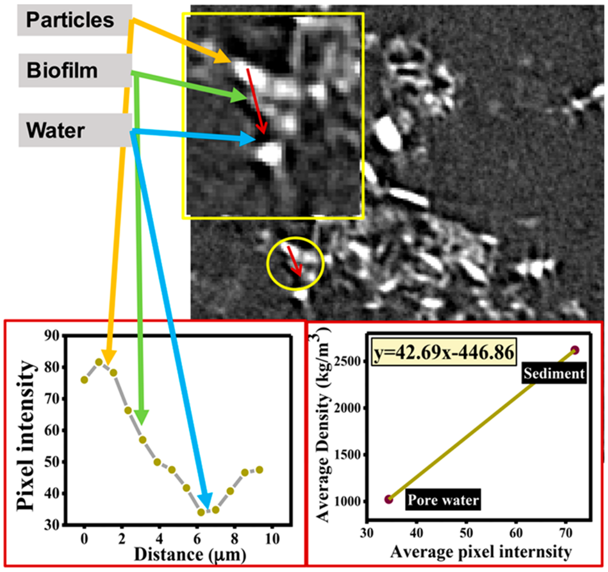

Figure 6. Example ROI containing all three different materials on the left-hand side. Each material shows a specific range of gray values: Inorganic sediment particles (orange arrows) represent the highest gray value range, while the intensity of pore water (blue arrows) shows a slightly lower intensity than biofilms (green arrows). The calibration of the linear relationship between intensity and density is illustrated in this selected ROI line.

To estimate the density of an aggregate rather than the detailed aggregate development mechanisms, the biofilm densities along each ROI line were then averaged, and the heterogeneous characteristics were simplified. As a result, each material component has one averaged density value. Accordingly,

$$d_f = \left(\sum_{i=1}^{n} d_i v_i\right) \Big/ \left(\sum_{i=1}^{n} v_i\right)$$

where d_f is the aggregate density, and d_i and v_i are the averaged density and volume of hydrated biofilm, sediment particles, and

DOI: 10.1021/acs.est.8b03997
Environ. Sci. Technol. 2018, 52, 13306−13313

pore water (the volume of each target component is calculated by counting the voxel number included in this component, each voxel volume is 0.777^3 nm^3), respectively.

To conclude, a method for 3D imaging aggregates and their multiphase components (including the discernment of biofilm matrix components) in hydrated form during a 3 h μ-CT scan is presented. This allows the observation of 3D biofilm-sediment binding geometries, and the calibration and estimation of individual aggregate densities, and has been assessed for replicability using duplicate scans. This method was tested and developed based on laboratory-cultivated aggregates but has also been used successfully to capture observations of hydrated biofilm matrix, inorganic particles, and pores in natural samples. Uncertainties remain when applying this method to natural samples: (1) it is uncertain whether this technique is applicable for distinguishing between different inorganic particles. Sophisticated prior calibration experiments might be required. (2) This method does not aim to distinguish individual microbial cells, such as algae cells or bacteria cells, but instead to capture the biofilm matrix with microbial cells embedded in an EPS matrix. Further work is required to elucidate the full capabilities of the methodology.

■ ASSOCIATED CONTENT

Ⓢ Supporting Information

The Supporting Information is available free of charge on the ACS Publications website at DOI: 10.1021/acs.est.8b03997.

> Animation of a hydrated BSA illustrating the sediment particles, hydrated biofilm matrix, and the biofilm-sediment binding in BSA as sustained in water (MPG)
>
> Micro-CT scanning protocols for each BSA sample, resulting scans of the LN2-frozen BSAs, irregular aggregate morphology by SEM, comparisons of the resulting scans of wet BSAs: unstained and stained, and calibration of the linear relationship between intensity and density and calculations of biofilm densities in 3 ROI lines examples (PDF)

■ AUTHOR INFORMATION

Corresponding Author

*Phone: +44(0)2380598467. E-mail: celt1@noc.soton.ac.uk.

Present Addresses

△C.E.L.T.: Channel Coastal Observatory, National Oceanography Centre, Southampton, SO14 3ZH, UK.

ORCID

Naiyu Zhang: 0000-0001-6000-786X

Notes

The authors declare no competing financial interest.

■ ACKNOWLEDGMENTS

This research was partially funded by the financial support of a Chinese student scholarship by the China Scholarship Council (CSC), and NERC award, NE/N015703/1. We gratefully acknowledge John Ford for his technical support for embedding specimens in resin, Dr. John R. Gittins for this technical support for Alcian blue staining solution preparation, and Ben Callow for his helpful advice in image processing. D.P. received funding from the Marine Alliance for Science and Technology for Scotland (MASTS), funded by the Scottish Funding Council (grant reference HR09011) and NERC awards, NE/J015644/1 and NE/1027223/1). A.J.M.'s contribution to this manuscript was partly funded by the HR Wallingford Company Research project 'FineScale - Dynamics of Fine-grained Cohesive Sediment at Varying Spatial and Temporal Scales' (DDY0523). We wish to extend thanks to Dr. Orestis Katsamenis and Dr. Richard Boardman for their assistance in performing the scans carried out at the μ-VIS X-ray Imaging Centre, University of Southampton (supported by EPSRC grant EP-H01506X).

■ REFERENCES

(1) Decho, A. W. Microbial Biofilms in Intertidal Systems: An Overview. *Cont. Shelf Res.* **2000**, *20* (10−11), 1257−1273.

(2) Flemming, H. C.; Wingender, J. The Biofilm Matrix. *Nat. Rev. Microbiol.* **2010**, *8* (9), 623−633.

(3) Schmitt, J.; Flemming, H. C. Water Binding in Biofilms. *Water Sci. Technol.* **1999**, *39*, 77−82.

(4) Fu, J.; Gong, Y.; Zhao, X.; O'Reilly, S. E.; Zhao, D. Effects of Oil and Dispersant on Formation of Marine Oil Snow and Transport of Oil Hydrocarbons. *Environ. Sci. Technol.* **2014**, *48* (24), 14392−14399.

(5) Milligan, T. G.; Law, B. A. Contaminants at the Sediment−Water Interface: Implications for Environmental Impact Assessment and Effects Monitoring. *Environ. Sci. Technol.* **2013**, *47* (11), 5828−5834.

(6) Witt, G.; Leipe, T.; Emeis, K. C. Using Fluffy Layer Material to Study the Fate of Particle-Bound Organic Pollutants in the Southern Baltic Sea. *Environ. Sci. Technol.* **2001**, *35* (8), 1567−1573.

(7) Perujo, N.; Sanchez-Vila, X.; Proia, L.; Romaní, A. M. Interaction between Physical Heterogeneity and Microbial Processes in Subsurface Sediments: A Laboratory-Scale Column Experiment. *Environ. Sci. Technol.* **2017**, *51* (11), 6110−6119.

(8) Gerbersdorf, S. U.; Wieprecht, S. Biostabilization of Cohesive Sediments: Revisiting the Role of Abiotic Conditions, Physiology and Diversity of Microbes, Polymeric Secretion, and Biofilm Architecture. *Geobiology* **2015**, *13* (1), 68−97.

(9) Rusconi, R.; Guasto, J. S.; Stocker, R. Bacterial Transport Suppressed by Fluid Shear. *Nat. Phys.* **2014**, *10* (3), 212−217.

(10) Passow, U. Formation of Rapidly-Sinking, Oil-Associated Marine Snow. *Deep Sea Res., Part II* **2016**, *129*, 232−240.

(11) Chen, X. D.; Zhang, C. K.; Paterson, D. M.; Thompson, C. E. L.; Townend, I. H. Hindered Erosion: The Biological Mediation of Non-Cohesive Sediment Behaviour. *Water Resour. Res.* **2017**, *53*, 4787.

(12) Vignaga, E.; Sloan, D. M.; Luo, X.; Haynes, H.; Phoenix, V. R.; Sloan, W. T. Erosion of Biofilm-Bound Fluvial Sediments. *Nat. Geosci.* **2013**, *6* (9), 770−774.

(13) Marzocchi, U.; Thamdrup, B.; Stief, P.; Glud, R. N. Effect of Settled Diatom-Aggregates on Benthic Nitrogen Cycling. *Limnol. Oceanogr.* **2018**, *63* (1), 431−444.

(14) Battin, T. J.; Kaplan, L. A.; Findlay, S.; Hopkinson, C. S.; Marti, E.; Packman, A. I.; Newbold, J. D.; Sabater, F. Biophysical Controls on Organic Carbon Fluxes in Fluvial Networks. *Nat. Geosci.* **2008**, *1* (2), 95−100.

(15) He, D.; Bligh, M. W.; Waite, T. D. Effects of Aggregate Structure on the Dissolution Kinetics of Citrate- Stabilized Silver Nanoparticles. *Environ. Sci. Technol.* **2013**, *47* (16), 9148−9156.

(16) Maggi, F.; Mietta, F.; Winterwerp, J. C. Effect of Variable Fractal Dimension on the Floc Size Distribution of Suspended Cohesive Sediment. *J. Hydrol.* **2007**, *343* (1−2), 43−55.

(17) Vahedi, A.; Gorczyca, B. Application of Fractal Dimensions to Study the Structure of Flocs Formed in Lime Softening Process. *Water Res.* **2011**, *45* (2), 545−556.

(18) Kranenburg, C. The Fractal Structure of Cohesive Sediment Aggregates. *Estuarine, Coastal Shelf Sci.* **1994**, *39* (6), 451−460.

(19) Mandelbrot, B. B. *The Fractal Geometry of Nature*, Revised and Enlarged Edition; New York, 1983.

(20) Manning, A. J.; Dyer, K. R. The Use of Optics for the in Situ Determination of Flocculated Mud Characteristics. *J. Opt. A Pure Appl. Opt.* **2002**, *4* (4), S71−S81.

(21) Stokes, G. G. On the Effect of the Internal Friction of Fluids on the Motion of Pendulums. *Trans. Cambridge Philos. Soc.* **1851**, *9*, 8−106.

(22) Ransom, B.; Shea, K. F.; Burkett, P. J.; Bennett, R. H.; Baerwald, R. Comparison of Pelagic and Nepheloid Layer Marine Snow: Implications for Carbon Cycling. *Mar. Geol.* **1998**, *150* (1−4), 39−50.

(23) Flemming, H. C. The Perfect Slime. *Colloids Surf., B* **2011**, *86* (2), 251−259.

(24) Wheatland, J. A. T.; Bushby, A. J.; Spencer, K. L. Quantifying the Structure and Composition of Flocculated Suspended Particulate Matter Using Focused Ion Beam Nanotomography. *Environ. Sci. Technol.* **2017**, *51* (16), 8917−8925.

(25) Paterson, D. M. Biogenic Structure of Early Sediment Fabric Visualized by Low-Temperature Scanning Electron Microscopy. *J. Geol. Soc.* **1995**, *152* (1), 131−140.

(26) Perkins, R. G.; Davidson, I. R.; Paterson, D. M.; Sun, H.; Watson, J.; Player, M. A. Low-Temperature SEM Imaging of Polymer Structure in Engineered and Natural Sediments and the Implications Regarding Stability. *Geoderma* **2006**, *134* (1−2), 48−55.

(27) Liss, S. N.; Droppo, I. G.; Flannigan, D. T.; Leppard, G. G. Floc Architecture in Wastewater and Natural Riverine Systems. *Environ. Sci. Technol.* **1996**, *30* (2), 680−686.

(28) Leppard, G. G.; Heissenberger, A.; Herndl, G. J. Ultrastructure of Marine Snow. I. Transmission Electron Microscopy Methodology. *Mar. Ecol.: Prog. Ser.* **1996**, *135* (1−3), 289−298.

(29) Romaní, A. M.; Giorgi, A.; Acuña, V.; Sabater, S. The Influence of Substratum Type and Nutrient Supply on Biofilm Organic Matter Utilization in Streams. *Limnol. Oceanogr.* **2004**, *49* (5), 1713−1721.

(30) Molins, S. Reactive Interfaces in Direct Numerical Simulation of Pore-Scale Processes. *Rev. Mineral. Geochem.* **2015**, *80*, 461−481.

(31) Keyes, S. D.; Daly, K. R.; Gostling, N. J.; Jones, D. L.; Talboys, P.; Pinzer, B. R.; Boardman, R.; Sinclair, I.; Marchant, A.; Roose, T. High Resolution Synchrotron Imaging of Wheat Root Hairs Growing in Soil and Image Based Modelling of Phosphate Uptake. *New Phytol.* **2013**, *198* (4), 1023−1029.

(32) Chu, C. P.; Lee, D. J. Multiscale Structures of Biological Flocs. *Chem. Eng. Sci.* **2004**, *59* (8−9), 1875−1883.

(33) Zhao, H.; Fang, H.; Chen, M. Floc Architecture of Bioflocculation Sediment by ESEM and CLSM. *Scanning* **2011**, *33* (6), 437−445.

(34) Landis, E. N.; Keane, D. T. X-Ray Microtomography. *Mater. Charact.* **2010**, *61* (12), 1305−1316.

(35) Wheatland, J.; Bushby, A.; Droppo, I.; Carr, S.; Spencer, K. Multi Length Scale Imaging of Flocculated Estuarine Sediments; Insights into Their Complex 3D Structure. In EGU General Assembly Conference Abstracts (Vol. *17*); 2015.

(36) Mietta, F.; Chassagne, C.; Winterwerp, J. C. Shear-Induced Flocculation of a Suspension of Kaolinite as Function of pH and Salt Concentration. *J. Colloid Interface Sci.* **2009**, *336* (1), 134−141.

(37) Thompson, C. E. L.; Williams, M. E.; Amoudry, L.; Hull, T.; Reynolds, S.; Panton, A.; Fones, G. R. Benthic Controls of Resuspension in UK Shelf Seas: Implications for Resuspension Frequency. *Cont. Shelf Res.* **2017**, 0−1.

(38) Droppo, I. G.; Flannigan, D. T.; Leppard, G. G.; Jaskot, C.; Liss, S. N. Floc Stabilization for Multiple Microscopic Techniques. *Appl. Environ. Microbiol.* **1996**, *62* (9), 3508−3515.

(39) Parker, P. J.; Collins, A. G. Ultra-Rapid Freezing of Water Treatment Residuals. *Water Res.* **1999**, *33* (10), 2239−2246.

(40) Chen, L. C.; Chian, C. Y.; Yen, P. S.; Chu, C. P.; Lee, D. J. High-Speed Sludge Freezing. *Water Res.* **2001**, *35* (14), 3502−3507.

(41) Metscher, B. D. Micro CT for Comparative Morphology: Simple Staining Methods Allow High-Contrast 3D Imaging of Diverse Non-Mineralized Animal Tissues. *BMC Physiol.* **2009**, *9*, 11.

(42) Hubbell, J. H.; Seltzer, S. M. *Tables of X-Ray Mass Attenuation Coefficients and Mass Energy-Absorption Coefficients 1 keV to 20 MeV for Elements Z = 1 to 92 and 48 Additional Substances of Dosimetric Interest*; 1995.

(43) Bar-Zeev, E.; Berman-Frank, I.; Girshevitz, O.; Berman, T. Revised Paradigm of Aquatic Biofilm Formation Facilitated by Microgel Transparent Exopolymer Particles. *Proc. Natl. Acad. Sci. U. S. A.* **2012**, *109* (23), 9119−9124.

(44) Thornton, D. C. O.; Visser, L. A. *Aquat. Microb. Ecol.* **2009**, *54* (February), 185−198.

(45) Passow, U.; De La Rocha, C. L.; Fairfield, C.; Schmidt, K. Aggregation as a Function of PCO2 and Mineral Particles. *Limnol. Oceanogr.* **2014**, *59* (2), 532−547.

(46) Amos, C. L.; Sutherland, T. F.; Radzijeski, B.; Doucette, M. A Rapid Technique to Determine Bulk Density of Fine-Grained Sediments by X-Ray Computed Tomography. *J. Sediment. Res.* **1996**, *66* (5), 1023−1024.

(47) Hale, R.; Boardman, R.; Mavrogordato, M. N.; Sinclair, I.; Tolhurst, T. J.; Solan, M. High-Resolution Computed Tomography Reconstructions of Invertebrate Burrow Systems. *Sci. Data* **2015**, *2*, 150052.

(48) Zhou, G.; Zhang, Q.; Bai, R.; Ni, G. Characterization of Coal Micro-Pore Structure and Simulation on the Seepage Rules of Low-Pressure Water Based on CT Scanning Data. *Minerals* **2016**, *6* (3), 78.

(49) Schindelin, J.; Arganda-Carreras, I.; Frise, E.; Kaynig, V.; Longair, M.; Pietzsch, T.; Preibisch, S.; Rueden, C.; Saalfeld, S.; Schmid, B.; Tinevez, J. Y.; White, D. J.; Hartenstein, V.; Eliceiri, K.; Tomancak, P.; Cardona, A. Fiji: An Open-Source Platform for Biological-Image Analysis. *Nat. Methods* **2012**, *9*, 676−682.

(50) Arganda-Carreras, I.; Kaynig, V.; Rueden, C.; Eliceiri, K. W.; Schindelin, J.; Cardona, A.; Seung, H. S. Trainable Weka Segmentation: A Machine Learning Tool for Microscopy Pixel Classification. *Bioinformatics* **2017**, *33* (15), 2424−2426.

(51) Callow, B.; Falcon-Suarez, I.; Ahmed, S.; Matter, J. Assessing the Carbon Sequestration Potential of Basalt Using X-Ray Micro-CT and Rock Mechanics. *Int. J. Greenhouse Gas Control* **2018**, *70* (August), 146−156.

(52) Avizo. Avizo 3D Software User's Guide. https://www.fei.com/software/avizo-user-guide/ (accessed Jul 7, 2017).

(53) Stone, M.; Krishnappan, B. G.; Emelko, M. B. The Effect of Bed Age and Shear Stress on the Particle Morphology of Eroded Cohesive River Sediment in an Annular Flume. *Water Res.* **2008**, *42* (15), 4179−4187.

(54) Winterwerp, J. C. A Simple Model for Turbulence Induced Flocculation of Cohesive Sediment. *J. Hydraul. Res.* **1998**, *36* (3), 309−326.

(55) Zhao, B.; Wang, J. 3D Quantitative Shape Analysis on Form, Roundness, and Compactness with μCT. *Powder Technol.* **2016**, *291*, 262−275.

(56) Tang, F. H. M. *Microbiological Modulation of Suspended Particulate Matter Dynamics: A Study of Biological Flocculation in Nutrient-Enriched Waters*, The University of Sydney.

(57) Alldredge, A. L.; Passow, U.; Logan, B. E. The Abundance and Significance of a Class of Large, Transparent Organic Particles in the Ocean. *Deep Sea Res., Part I* **1993**, *40* (6), 1131−1140.

(58) Nguyen, T. H.; Tang, F. H. M.; Maggi, F. Optical Measurement of Cell Colonization Patterns on Individual Suspended Sediment Aggregates. *J. Geophys. Res. Earth Surf.* **2017**, *122*, 1794−1807.

(59) Kamaruddin, N.; Rajion, Z. A.; Yusof, A.; Aziz, M. E. Relationship between Hounsfield Unit in CT Scan and Gray Scale in CBCT. *AIP Conf. Proc.* **2016**, *1791*, 020005.

(60) Amos, C. L.; Bergamasco, A.; Umgiesser, G.; Cappucci, S.; Cloutier, D.; Denat, L.; Flindt, M.; Bonardi, M.; Cristante, S. The Stability of Tidal Flats in Venice Lagoon - The Results of in-Situ Measurements Using Two Benthic, Annular Flumes. *J. Mar. Syst.* **2004**, *51* (1−4 SPEC. ISS.), 211−241.

(61) Orsi, T. H. Computed Tomography of Macrostructure and Physical Property Variability of Seafloor Sediments. *Oceanography* **1995**, *8*, 61−64.

DOI: 10.1021/acs.est.8b03997
Environ. Sci. Technol. 2018, 52, 13306−13313